Nanoscale Advances

ROYAL SOCIETY OF CHEMISTRY

PAPER

View Article Online
View Journal | View Issue

Cite this: *Nanoscale Adv.*, 2023, **5**, 3063

Hollow @CuMgAl double layered hydrotalcites and mixed oxides with tunable textural and structural properties, and thus enhanced NH_3-NO_x-SCR activity

Tomasz Kondratowicz, *[ab] Ondřej Horký,[a] Stanislav Slang, [c] Lada Dubnová, [a] Marta Gajewska,[d] Lucjan Chmielarz[e] and Libor Čapek *[a]

Well-organized, spherical, mesoporous hollow @CuMgAl-LDHs (layered double hydroxides) are prepared by the controlled removal of the SiO_2 from SiO_2@CuMgAl-LDH core–shell hybrids that in turn are synthesized *via* a bottom-up strategy. The materials are prepared with various Cu/Mg molar ratios (Cu/Mg = 0.05–0.50) while keeping the ratio of Cu and Mg constant, (Cu + Mg)/Al = 2. The effect of Cu doping and the silica core removal process (conducted for 4 h at 30 °C using 1 M NaOH) on the chemical composition, morphology, structure, texture and reducibility of the resulting materials are described. @CuMgAl-MOs (mixed oxides) obtained by thermal treatment of the @CuMgAl-LDHs are active and selective catalysts for the selective catalytic reduction of NO_x using ammonia, and effectively operate at low temperatures. The N_2 yield increases with increased Cu content in the CuMgAl shell, which is associated with the easier reducibility of the Cu species incorporated into the MgAl matrix. @CuMgAl-MOs show better catalytic performance than bulk CuMgAl MOs.

Received 27th February 2023
Accepted 26th April 2023

DOI: 10.1039/d3na00125c

rsc.li/nanoscale-advances

Introduction

NO_x is primarily made up of nitric oxide (NO) and nitrogen dioxide (NO_2) and belongs to a significant group of air pollutants which have a number of negative impacts on human health and the environment, including *e.g.*, photochemical smog, ozone depletion and acid rain.[1] The anthropogenic emission of NO_x originates mainly from the stationary combustion of fossil fuels, such as that found in steel plants, power plants, cement plants and waste incineration. NO_x emissions also originate from mobile sources, with a major contribution from the use of diesel engines. Considering the above, NO_x emissions should be reduced by 42% for all EU member countries over the years 2020–2029.[2]

Up to now, the most recognized and effective technology for NO_x abatement is the selective catalytic reduction of NO_x using ammonia (NH_3-SCR), urea, or hydrocarbons (HC-SCR).[3] Commercial NH_3-SCR technology has been implemented in thermal power plants using V_2O_5-$WO_3(MoO_3)$/TiO_2 catalysts with relatively high efficiency in the temperature range of 300–400 °C.[4] However, exhaust gas temperatures in non-energy industries are often much lower, rendering vanadium-based SCR catalysts less efficient. Therefore, the development of catalysts with a satisfactory low-medium temperature catalytic activity window (<250 °C) and good resistance stability (*e.g.*, in the presence of SO_2 or HCl) is a permanent challenge for chemists and materials scientists for both economic and environmental reasons.[4–6] Among the many proposed systems, metal oxides, such as Cu,[7,8] Fe[9,10] and Mn,[11,12] are widely recognized and considered to be effective active components for low-medium temperature SCR catalysts, mainly due to their high catalytic activity, long lifetimes, wide availability and relatively low production costs. Besides the qualitative composition of the catalysts, the transition metal content also greatly influences the efficiency in the NH_3-SCR process.[13–15] However, synthesis of multicomponent oxide catalysts by traditional preparation methods, *e.g.*, coprecipitation, hydrothermal synthesis and sol–gel methods, often leads to a heterogeneous distribution of the active components, as well as agglomeration and sintering of particles, which may significantly limit the potential of these catalysts for practical applications.[1]

Therefore, mixed oxides (MOs) originating from layered double hydroxides (LDHs) with different combinations of metal ions have been successfully tested as SCR catalysts since the late

[a]*University of Pardubice, Faculty of Chemical Technology, Department of Physical Chemistry, Studentská 573, 532 10 Pardubice, Czech Republic. E-mail: tomasz.kondratowicz@chem.ox.ac.uk; libor.capek@upce.cz*

[b]*Chemistry Research Laboratory, Department of Chemistry, University of Oxford, 12 Mansfield Road, Oxford, OX1 3TA, UK*

[c]*University of Pardubice, Faculty of Chemical Technology, Center of Materials and Nanotechnologies, Studentská 95, 532 10 Pardubice, Czech Republic*

[d]*Academic Centre for Materials and Nanotechnology, AGH University of Science and Technology, Mickiewicza 30, 30-059 Kraków, Poland*

[e]*Jagiellonian University, Faculty of Chemistry, Gronostajowa 2, 30 387 Kraków, Poland*

1990s.[1] Such great interest in this class of materials is related to their unique properties, such as having excellent and uniform metal oxide dispersions, high thermal stabilities and memory effects. Moreover, their properties and surface compositions can be easily tuned during the synthesis, their preparation methods are well known, and they are environmentally friendly materials that are relatively cheap to produce. However, frequently LDH materials prepared using conventional methods have poor morphologies, such as aggregated powders composed of irregular particles of various sizes (stone-like morphologies).[16] This is the result of severe platelet aggregation caused by *ab*-face stacking during the drying process and it may negatively affect the porosity of the LDH materials and significantly limits their utilization.

Given the unique and important properties of pristine LDHs and MOs, various functionalization strategies have been applied to bring even more exciting performance outcomes. One such strategy is the dispersion of LDHs *via* aqueous miscible organic solvent treatment (AMOST) into thin nanosheets or *via* exfoliation into single layers.[17,18] Another class of LDHs modification is the generation of additional porosity, and thus a significant expansion of the specific surface area, in pristine LDHs, which enables better dispersions of the LDHs, exposes more active sites and facilitates the mass transport of reagents towards and from the surface. This goal can be achieved through alkaline etching that utilizes the amphoteric features of the Al^{3+} ion in the LDHs crystal[19,20] or by the introduction of a foreign substance during the synthesis of the LDH materials. The synthesis can be performed in the presence of carbon-containing precursors, such as activated carbon,[21] date palm ash,[22] and all types of ionic and non-ionic surfactant molecules,[23–26] which can then be removed by thermal treatment, helping to fine-tune the surface properties of the resulting mixed oxides.

In addition to the above-mentioned methods to tailor LDHs, approaches based on the immobilization of LDH on supports is a relatively new field of materials chemistry, proposed for the first time by Zhang *et al.* in 2009.[27] In particular, when hard templates with well-defined shapes and dimensions are employed, three-dimensional (3D) hierarchical LDH-based materials can be constructed to further improve the diffusion limitations, accessibility of the active sites, texture properties as well as the irregular shapes and sizes of the LDHs.[28,29] Up to now, various types of LDH-based core–shell nanostructures with a variety of cores have been reported, *e.g.*, nonporous SiO_2,[30] mesoporous silicas (*e.g.*, MCM-41, MCM-48, SBA-15),[31] Fe_xO_y,[32] Cu_2O,[33] TiO_2,[34] zeolites (*e.g.*, ZSM-5, Y, TS-1),[35] MOFs[36] and carbon.[37]

However, the current state of the literature clearly shows that SiO_2@MgAl-LDH hybrids[16,30,38–44] are the most explored and well-described in the literature. This is probably related to (i) the relatively fast and uncomplicated synthesis of the spherical SiO_2 core with tunable control of particle size using the Stöber process,[45] (ii) the high stability of the SiO_2@LDH composite due to the Si–O–M covalent bonds,[46] as well as (iii) the MgAl phase being among the most popular variety of LDHs. A few papers have described other SiO_2@LDH core–shell systems in which the LDH consists of NiAl,[39,47,48] NiFe, CoFe, CoNi[47] and MgGa.[39] However, core–shell materials containing silica as a core and more than two elements in the LDH shell have not been thoroughly examined. To date, only three structures, SiO_2@CeMgAl-LDH,[49] SiO_2@MgAlFe-LDH and SiO_2@MgAlNi-LDH,[50] have been described in detail.

The study focusses on hollow @CuMgAl-LDHs and hollow @CuMgAl-MOs and is a natural continuation and extension of our previous work,[38] in which we presented a controlled removal of the SiO_2 core from a SiO_2@MgAl-LDH system to form hollow @MgAl-LDHs. Additionally, this work perfectly fills the space describing core–shell systems containing a SiO_2 core and ternary LDHs as a shell. SiO_2@CuMgAl-LDHs materials with various Cu/Mg molar ratios (0.05–0.50) are synthesized while keeping the (Cu + Mg)/Al molar ratio at a constant value of 2. Additionally, the conditions for the SiO_2 core removal which facilitate the formation of hollow @CuMgAl-LDH are described. The effect of doping MgAl-LDH with various amounts of Cu, the implementation of the silica core removal process and the effect of thermal treatment (to form mixed oxides) on the morphology, structural, textural and redox properties of the core–shell and hollow sphere materials are described here. Moreover, the potential of such materials in environmental catalysis (selective catalytic reduction of NO with ammonia (NH_3-SCR)) has also been demonstrated.

Experimental

Synthesis

The spherical core–shell SiO_2@CuMgAl-LDH materials (with various Cu/Mg molar ratios with a constant Cu + Mg/Al ratio of 2) were prepared according to our previous work.[38] The method involves the *in situ* coprecipitation of Cu, Mg and Al precursors in the presence of non-porous spherical SiO_2 particles of uniform size with *ca.* 400 nm diameters. Briefly, 100 mg of spherical SiO_2 particles were dispersed in 20.0 mL of deionized water using an ultrasound bath. After 1 h, 0.96 mmol of Na_2CO_3 (Lach-Ner, 100.1%) was added to the milky solution and dispersed for another 10 minutes. Subsequently, to the as-prepared suspension was added dropwise (1 mL min^{-1}) a 19.2 mL water solution containing various amounts of $Cu(NO_3)_2 \cdot 3H_2O$ (Lach-Ner, 101.9%), $Mg(NO_3)_2 \cdot 6H_2O$ (Lach-Ner, 100.8%), and $Al(NO_3)_3 \cdot 9H2O$ (Lach-Ner, 98.6%) (total metal concentration = 1.44 mmol). The pH was maintained at 10.00 ± 0.03 using an aqueous NaOH solution (1 M) during titration. After 2 h of stirring (400 rpm), the obtained core–shell particles were filtered, washed with 2 L of deionized water and dried at 60 °C overnight. Dried samples are denoted as SiO_2@CuMgAl_*x*-LDH, where *x* expresses the nominal Cu/Mg molar ratio (0.05, 0.1, 0.2, 0.3, 0.4 and 0.5).

In the next step, the silica core was etched under static conditions by treatment with a NaOH solution (1 M) at 30 °C for 4 h. To remove remaining NaOH, the obtained particles were thoroughly washed with distilled water (2 L) and then dried at 60 °C. The obtained materials are denoted as @CuMgAl_*x*-LDH.

CuMgAl-based mixed oxides were obtained by thermal treatment of the LDH-like precursor in air at 450 °C for 4 h (heating rate of 5 °C min^{-1}) in a muffle oven. Calcined materials are denoted as @CuMgAl_*x*-MO.

Characterization

Quantitative energy-dispersive X-ray spectroscopy (EDX) measurements were performed on an electron microscope (LYRA3, Tescan) equipped with an EDX analyzer AZtec X-Max 20 (Oxford Instruments) at an acceleration voltage of 20 kV (an accelerating voltage possessing a signal from a depth of micrometres, which is sufficient for the studied core–shell particles with dimensions of approximately 800 nm). The samples were covered with 20 nm of carbon using a Leica EM ACE200 coater and subsequently 5 different spots with a size of 200 × 200 μm were measured and the obtained compositions were averaged. A scanning electron microscope (LYRA3, Tescan) was used for the surface morphology study using a 10 kV acceleration voltage. The samples were coated with a thin 18 nm layer of gold (Leica EM ACE200) prior to the scanning electron microscopy (SEM) analysis. Transmission electron microscopy (TEM) measurements were carried out on a FEI Tecnai TF20 X-TWIN (FEG) microscope equipped with an energy-dispersive X-ray spectrometer (EDAX), working at an accelerating voltage of 200 kV. Samples for the TEM observations were prepared by drop-casting on carbon-coated copper grids. The crystallographic structure of samples was determined using a Rigaku MiniFlex 600 diffractometer with a PDF-2 database and D/teX Ultra detector using Cu Kα radiation operated at 40 kV and 15 mA. The X-ray diffraction (XRD) patterns were recorded in the range of 2θ = 5–80° with a step of 0.02°. Nitrogen adsorption–desorption isotherms were recorded at −196 °C using a Micromeritics TriStar II instrument. Before the measurements, samples were degassed for 6 h under vacuum at 130 °C or 150 °C for the LDH and MO phases, respectively. Specific surface areas (S_{BET}) were determined using the Brunauer–Emmett–Teller (BET) method. Total pore volumes (V_{total}) were obtained from the amounts of nitrogen adsorbed at a relative pressure of 0.99, whereas the micropore (V_{micro}) and mesopore (V_{meso}) volumes were calculated using a *t*-plot and Barrett–Joyner–Halenda (BJH) models, respectively. In turn, the volume of macropores (V_{macro}) was calculated as the difference between V_{total} and the sum of V_{micro} and V_{meso}. Temperature-programmed reduction with hydrogen (H_2-TPR) was carried out in a flow system using a Micromeritics AutoChem II 2920 equipped with a TCD detector. Before a TPR experiment, 100 mg of a sample was outgassed in a flow of helium (25 mL min^{-1}) at 450 °C and then for 30 min in an oxygen atmosphere at 450 °C, followed by cooling to 150 °C. At 150 °C, the oxygen atmosphere was swapped to a helium atmosphere to flush the reactor with an inert gas and the reactor was cooled down to 25 °C. After a freezer was added to the system, the hydrogen uptake from a stream of 5 vol% of H_2 in Ar (a flow rate of 25 mL min^{-1}) was analyzed over a temperature range of 25–900 °C at a heating rate of 10 °C min^{-1}. The number of redox sites was calculated from the integrals of the signal after their integration with external calibration.

Catalytic tests

The catalysts were tested in the selective catalytic reduction of NO with ammonia (NH_3-SCR). Catalytic studies were performed on an experimental system consisting of a fixed-bed quartz microreactor with the outlet connected directly to the detector – a quadrupole mass spectrometer (QMS, PREVAC). The used gas mixture contained 0.25 vol% NO, 0.25 vol% NH_3 and 2.5 vol% O_2 diluted in pure helium (total flow rate of 40 mL min^{-1}). Prior to the catalytic run, 100 mg of the sample (particle size in the range of 250–315 μm) was placed in the quartz microreactor and outgassed in the flow of pure helium at 450 °C for 30 min. After the microreactor was cooled down to 100 °C, the catalytic test was initiated with a linear heating rate of 10 °C min^{-1}, over a temperature range of 100–400 °C. Catalytic tests were performed under atmospheric pressure.

Moreover, for the most active catalyst, an isothermal long-term stability NH_3-SCR test at 275 °C for 24 h was done with the same composition of the reaction mixture and mass of the catalyst sample. A catalytic study of the ammonia oxidation reaction was carried out using the same experimental system used in the case of the NH_3-SCR tests. Prior to the catalytic tests, the samples (100 mg, particle sizes of 250–315 μm) were outgassed in a flow of pure helium (20 mL min^{-1}) at 450 °C for 30 min. Catalytic runs were conducted in the temperature range of 100–450 °C with a gas mixture containing: $[NH_3]$ = 0.5 vol% and $[O_2]$ = 2.5 vol%, diluted in pure helium used as a balance gas (total flow rate 40 mL min^{-1}). All catalytic experiments were performed at a constant gas hourly space velocity (GHSV) and a volumetric hourly space velocity (VHSV) of approx. 12 000 h^{-1} and 24 000 cm^3 h^{-1} g^{-1}, respectively.

Results and discussion

Features of the spherical SiO_2@CuMgAl-LDH and @CuMgAl-LDHs

Table 1 gives the Cu/Mg, (Cu + Mg)/Al and the Si/(Si + Cu + Mg + Al) molar ratios of the pristine core–shell SiO_2@CuMgAl-LDHs and the hollow @CuMgAl-LDHs obtained after the leaching of the SiO_2 core for 4 h. To keep a constant (Cu + Mg)/Al molar ratio, magnesium was isomorphically substituted by copper during the synthesis. However, the experimental Cu/Mg and (Cu + Mg)/Al molar ratios for the SiO_2@CuMgAl-LDHs were slightly

Table 1 Chemical composition of the SiO_2@MgAl-LDH core–shell materials before and after NaOH leaching

Sample	Cu/Mg	(Cu + Mg)/Al	Si/(Si + Cu + Mg + Al)
SiO_2@CuMgAl_0.05-LDH	0.07	2.04	0.52
SiO_2@CuMgAl_0.10-LDH	0.12	2.04	0.50
SiO_2@CuMgAl_0.20-LDH	0.25	2.12	0.48
SiO_2@CuMgAl_0.30-LDH	0.39	2.16	0.47
SiO_2@CuMgAl_0.40-LDH	0.50	2.18	0.47
SiO_2@CuMgAl_0.50-LDH	0.60	2.15	0.48
@CuMgAl_0.05-LDH	0.06	2.06	0.14
@CuMgAl_0.10-LDH	0.12	2.07	0.21
@CuMgAl_0.20-LDH	0.24	2.06	0.26
@CuMgAl_0.30-LDH	0.35	2.11	0.16
@CuMgAl_0.40-LDH	0.45	2.11	0.17
@CuMgAl_0.50-LDH	0.56	2.11	0.28

higher than the theoretical values. Similar discrepancies between the theoretical and real Cu/Mg molar ratios in LDHs have been reported previously in the literature.[51–54] The observed differences may result from the preferential incorporation of Cu^{2+} ions into the crystal lattice during the growth of the LDH phase over Mg^{2+} ions. It could be connected with the pH value, as the coprecipitation of various ions requires different pH values.[55] Thus, the pH value of 10.0, used in the synthesis of SiO_2@CuMgAl-LDHs, could slightly favour the incorporation of Cu^{2+} ions. It can also be explained by the preferential dissolution of the Mg^{2+} ions over Cu^{2+} during the washing of the solid materials with water. This hypothesis may be supported by the fact that $Mg(OH)_2$ is about 3 orders of magnitude more water-soluble than $Cu(OH)_2$ (the solubility equilibrium at 25 °C is 5.61×10^{-12} *vs.* 1.99×10^{-20}, respectively). Additionally, the partial dissolution of Al^{3+} and Cu^{2+} in NaOH solution, due to their amphoteric properties, cannot be excluded.[19,20,56] However, considering the relatively low NaOH concentration used during the modification, the impact may by negligible. In our previous study,[38] it was reported that the silica core cannot be completely removed from the SiO_2@MgAl-LDHs even at long leaching times (up to 48 h) or at much stronger leaching conditions (2 M, 50 °C, 20 h). For the synthesis of @MgAl-LDHs, the optimal conditions chosen for the leaching of the SiO_2 core with respect to its catalytic behaviour were a 1 M NaOH solution for 4 h. Therefore, based on that, the same conditions for leaching the SiO_2 core of SiO_2@CuMgAl-LDHs were implemented. It is a compromise between the degree of silica core removal from the core–shell system on one side, and the resulting morphology, textural, basic and catalytic properties on the other. For the pristine SiO_2@CuMgAl-LDHs, the Si/(Si + Cu + Mg + Al) molar ratio was in the range of 0.47–0.52 (Table 1). After 4 h of SiO_2 template leaching, the Si/(Si + Cu + Mg + Al) molar ratio decreased, and it was found to range from 0.14 to 0.28. It should be emphasized that despite application of the same conditions (4 h, 1 M NaOH), it was not possible to achieve the same level of the SiO_2 core removal for all the @CuMgAl-LDHs (Table 1).

Fig. 1A and B show XRD patterns of the SiO_2@CuMgAl-LDHs and @CuMgAl-LDHs, respectively. Also shown is the diffractogram of the reference material CuMgAl_ref-LDH. The XRD patterns of all materials contained diffraction lines at 11.6°, 23.4°, 34.8°, 39.2°, 46.8°, 60.6° and 62.0° that could be assigned to the (0 0 3), (0 0 6), (0 1 2), (0 1 5), (0 1 8), (1 1 0) and (1 1 3) planes, respectively, typical for classical double-layered structures with the trigonal $R\bar{3}m$ space group.[57,58] The shape of the diffraction lines does not vary significantly with increasing copper content (Cu/Mg molar ratio), neither in intensity nor in peak position shift. Moreover, for the pristine SiO_2@CuMgAl-LDHs, a broad hump at $2\theta \approx 22°$ is distinctly visible and is related to the presence of the amorphous SiO_2 core in the core–shell particles.[38,59] After 4 h of alkali treatment, none of the positions of the LDH diffraction lines change, while their intensities slightly increased, and the broad hump almost disappears (the slight bend in the baseline between the (003) and (012) planes is still visible). This confirms a decrease in the silica content of the @CuMgAl-LDHs relative to their corresponding pristine structures. Table 2 contains the lattice parameters a ($a = 2d_{110}$), c ($c = 3d_{003}$), LDH basal spacing (also known as the d value or interlayer distance along the c axis, calculated from $d(003)$[60]) as well as the LDH crystallite size in the stacking direction $D(003)$ and plane direction $D(110)$. The lattice parameters and LDH basal spacings are almost identical for all SiO_2@CuMgAl-LDHs regardless of the LDH composition. Additionally, these parameters were maintained around the same values in the @CuMgAl-LDHs (after leaching of the SiO_2 core for 4 hours). The determined unit cell in the crystal lattice and the d value for the SiO_2@CuMgAl-LDHs and hollow @CuMgAl-LDHs correspond to the previously reported SiO_2@-MgAl-LDHs and hollow@MgAl-LDHs[38] as well as other classic bulk double-layered structures with the similar M^{2+}/Al^{3+} molar ratios.[60,61] This may be explained by the almost identical sizes of the octahedral ionic radii of Cu^{2+} (0.73 Å) and Mg^{2+} (0.72 Å).[62] On the other hand, the calculated unit cell dimensions are slightly lower than those of various SiO_2@LDH core–shell systems (LDH = MgAl, NiAl, MgGa, $M^{2+}/M^{3+} = 3$).[39,40] This difference may be explained by the different ionic radii in the

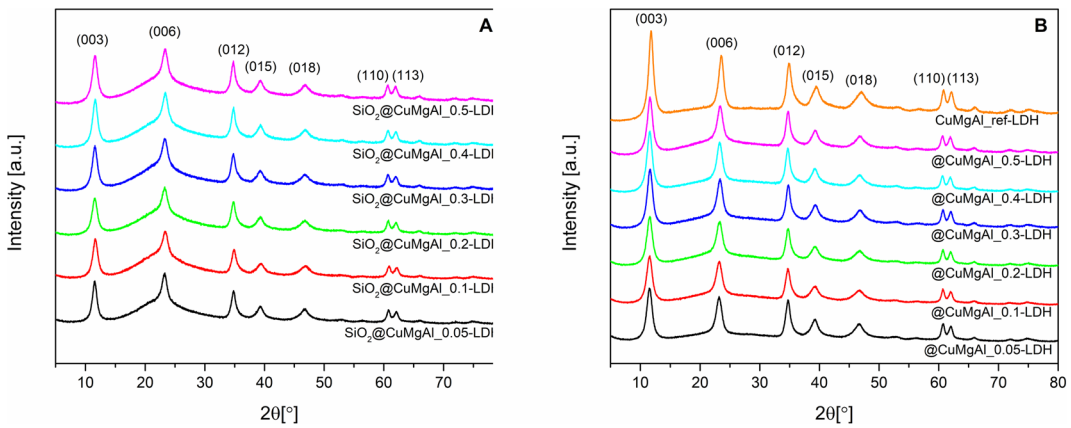

Fig. 1 XRD patterns of the SiO_2@CuMgAl-LDH composites (A) before and (B) after SiO_2 core etching with 1 M NaOH solution. A pattern for a CuMgAl-LDH reference sample is also shown.

Table 2 Crystallographic properties of the SiO_2@CuMgAl-LDH systems before and after leaching

	Lattice parameters [nm]		LDH basal spacing [nm]	Crystallite size [nm]	
Sample	*a*	*c*	*d*	*D*(003)	*D*(110)
SiO_2@CuMgAl_0.05-LDH	0.305	2.291	0.764	7.8	12.7
SiO_2@CuMgAl_0.1-LDH	0.304	2.297	0.766	7.7	13.2
SiO_2@CuMgAl_0.2-LDH	0.305	2.299	0.766	7.0	13.1
SiO_2@CuMgAl_0.3-LDH	0.305	2.293	0.764	7.5	13.0
SiO_2@CuMgAl_0.4-LDH	0.305	2.295	0.765	7.1	12.3
SiO_2@CuMgAl_0.5-LDH	0.305	2.295	0.765	6.9	12.6
@CuMgAl_0.05-LDH	0.305	2.297	0.766	7.2	13.9
@CuMgAl_0.1-LDH	0.305	2.300	0.767	6.9	14.0
@CuMgAl_0.2-LDH	0.305	2.293	0.764	6.6	14.6
@CuMgAl_0.3-LDH	0.305	2.290	0.763	7.2	14.7
@CuMgAl_0.4-LDH	0.306	2.293	0.764	7.0	14.4
@CuMgAl_0.5-LDH	0.305	2.285	0.762	7.1	13.4

other systems as well as higher molar ratio between M^{2+} and M^{3+} in the brucite-like layers. In the case of the LDH crystallite size in the SiO_2@CuMgAl-LDHs, the calculated dimension in the stacking direction *D*(003) is slighter shorter than in the plane direction *D*(110) and are in the range of 6.9–7.8 and 12.3.1–13.2 nm, respectively. After treatment in an alkaline environment, these values remained almost unchanged in the @CuMgAl-LDHs (6.6–7.2 and 13.4–14.7 nm, respectively). Crystallite sizes that are higher in the plane direction than in the stacking direction have also been reported for other core–shell materials constructed with SiO_2 cores and NiAl-, MgGa-,[39] and MgAl-LDH[38–40] shells. Previously reported CuMgAl-LDHs with a similar composition (Cu/Mg = 0.08 and (Cu + Mg)/Al = 2.03) and synthesized *via* a co-precipitation method, but without the SiO_2 particles, resulted in much higher crystallite sizes (75 nm).[53] The rapid nucleation of LDH compactly packed on the surface of the core, with simultaneous faster growth of the LDH crystal on the (110) plane than on the (003) plane, is known to ensure vertical orientation of the LDH plates onto the surface of the support.[46,63] Consequently, it is suggested that the CuMgAl-LDH platelets are anchored perpendicularly onto the SiO_2 surface in the SiO_2@CuMgAl-LDH core–shell materials.

Regardless of the composition of the CuMgAl-LDH in the SiO_2@CuMgAl-LDHs core–shell particles, no considerable changes in their shape and size were observed using microscopic techniques. Therefore, SEM and TEM images were obtained for the material with the highest Cu content, *i.e.*, SiO_2@CuMgAl_0.5-LDH (Fig. 2A and B, respectively). The prepared core–shell structures are evenly covered by the LDH phase with the CuMgAl-LDH platelets oriented mainly perpendicularly on the SiO_2 template surface. The smooth surface of the SiO_2 is not visible in any case. Moreover, the material shows uniform size distribution with an average diameter of the particles of *ca.* 800 nm and a thickness of the CuMgAl-LDH shell of ≈150 nm (estimated from more than 70 particles). After partial leaching of the SiO_2 core from the SiO_2@CuMgAl-LDHs for 4 h, a significant change of morphology is observed in the resulting @CuMgAl-LDH materials due to a decrease of the Si/(Si + Cu + Mg + Al) molar ratio (Fig. 2C and D). The formed hollow @CuMgAl-LDH spheres do not collapse, retaining their original spherical shape derived from the core–shell system, although a certain part of spheres is cracked with an obviously visible void inside the grains. The possible causes of these cracks were considered previously.[38] The most likely explanation comes from the fact that the shells could have been formed on two or more silica spheres that were close to each other (in aggregated forms), thus blocking LDH growth in the space between the balls (contact surface). In such cases, a more complex system exists resembling, *e.g.*, a raspberry-like shape, and after SiO_2 leaching and/or pulverizing in a mortar, may burst, resulting in visibly broken, empty shells. Additionally, a change in the contrast between the core and the shell is visible (Fig. 2B and D) as a result of the partial removal of the SiO_2 from the materials (Si/(Si + Cu + Mg + Al) molar ratio decreased from 0.48 to 0.28). Moreover, the above-mentioned diversity (between the core and shell of the core–shell and hollowed particles) is slightly less visible than was the case in our last study,[38] where TEM images of an analogous system (@MgAl-LDH with a Si/(Si + Mg + Al) molar ratio of 0.11) were studied. Additionally, a similar effect was also reported by Chen *et al.*,[16] who investigated the influence of the SiO_2@MgAl-LDH synthesis conditions (temperature, pH) on the formation of core–shell, yolk–shell and hollow particles. However, the authors did not provide the chemical composition of the different types of spherical particles formed but suggested that the interface between the SiO_2 and LDH phases is more stable than the silica in the core.

The isotherms for the SiO_2@CuMgAl-LDHs and @CuMgAl-LDHs are shown in Fig. 3A and B, respectively, and the determined textural parameters are presented in Table 3. All SiO_2@-CuMgAl-LDH core–shell particles show IVa type N_2 adsorption isotherms, according to the IUPAC classification, with H3 hysteresis loops characteristic for mesoporous materials with slit-shape pores.[64] Regardless of the amount of copper introduced, the volume of the mesopores was similar (0.18–0.19 $cm^3\ g^{-1}$), and the total pore volume ranged from 0.32 to 0.39 $cm^3\ g^{-1}$. The specific surface area of the core–shell systems slightly increases with an increase in the Cu/Mg molar ratio (from 76 to 84 $m^2\ g^{-1}$). This correlates with the lowest specific surface area of SiO_2@MgAl-LDH

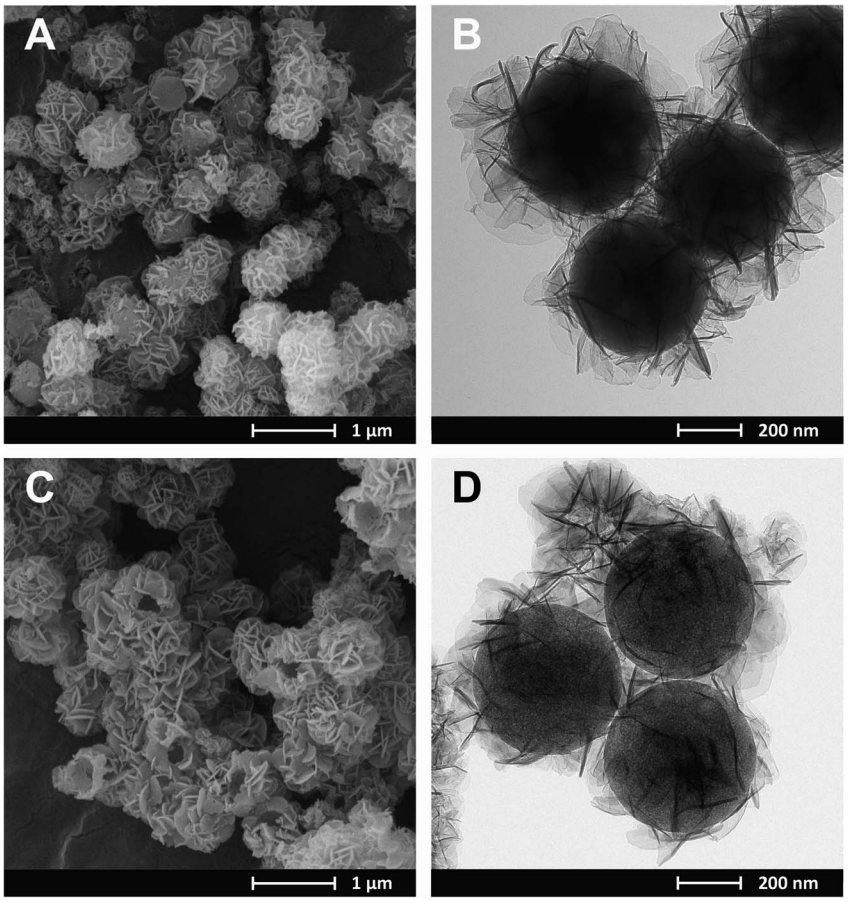

Fig. 2 SEM and TEM images of SiO_2@CuMgAl-LDH (A, B) and @CuMgAl-LDH (C, D).

(without Cu, 65 $m^2\ g^{-1}$).[38] Considering that (i) the silica core is a non-porous solid ($S_{BET} \approx 10\ m^2\ g^{-1}$)[38] and (ii) that the influence it has on the textural properties of all the SiO_2@CuMgAl-LDH core–shell materials is similar in all cases, its impact on the above trend can be ignored. Thus, the growth of the specific surface area of the core–shell systems as the Cu/Mg molar ratio increases can only be attributed to the LDH phase. The partial elimination of silica, reached after 4 hours of etching, results in an opening of the pore structure. This effect was observed in the measured isotherms as the significant increase in the volume of N_2 adsorbed (especially noticeable at relatively low p/p_0) and should be related to the appearance of new pores in the @CuMgAl-LDH materials. The values of $V_{total} = 0.66–0.71\ cm^3\ g^{-1}$, $V_{meso} = 0.39–0.47\ cm^3\ g^{-1}$ and $V_{macro} = 0.21–0.28\ cm^3\ g^{-1}$ demonstrated in Table 3 confirm this hypothesis. For the sake of completeness, it should be mentioned that the micropore volume for @CuMgAl-LDHs also increased by 2 to 3 times compared to the pristine core–shell materials, but the determined volume

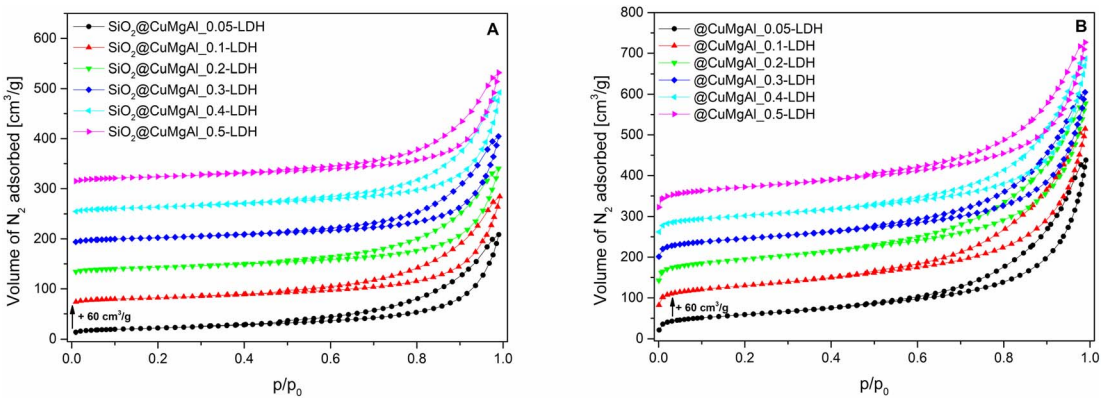

Fig. 3 N_2 adsorption isotherms for the SiO_2@CuMgAl-LDH composites (A) before and (B) after SiO_2 core etching.

Table 3 Textural properties of the SiO_2@CuMgAl-LDH and @CuMgAl-LDH materials

Sample	S_{BET} [m^2 g^{-1}]	V_{micro} [cm^3 g^{-1}]	V_{meso} [cm^3 g^{-1}]	V_{macro} [cm^3 g^{-1}]	V_{total} [cm^3 g^{-1}]
SiO_2@CuMgAl_0.05-LDH	76	0.007	0.180	0.135	0.322
SiO_2@CuMgAl_0.1-LDH	78	0.006	0.188	0.152	0.347
SiO_2@CuMgAl_0.2-LDH	80	0.007	0.188	0.143	0.340
SiO_2@CuMgAl_0.3-LDH	79	0.007	0.181	0.159	0.347
SiO_2@CuMgAl_0.4-LDH	83	0.007	0.190	0.193	0.390
SiO_2@CuMgAl_0.5-LDH	84	0.007	0.189	0.162	0.358
@CuMgAl_0.05-LDH	210	0.013	0.389	0.276	0.677
@CuMgAl_0.1-LDH	251	0.015	0.474	0.214	0.703
@CuMgAl_0.2-LDH	270	0.017	0.443	0.247	0.707
@CuMgAl_0.3-LDH	236	0.019	0.387	0.251	0.657
@CuMgAl_0.4-LDH	222	0.018	0.392	0.280	0.691
@CuMgAl_0.5-LDH	258	0.021	0.384	0.255	0.660

(0.01–0.02 cm^3 g^{-1}) has a negligible effect on the total porosity of the studied materials. The formation of new pores affected the specific surface area, which increased to 210–270 m^2 g^{-1}. However, an interesting correlation between S_{BET} and the chemical composition of the @CuMgAl-LDH systems was found (Fig. 4). Materials with the nominal Cu/Mg molar ratios of 0.05, 0.30 and 0.40 (group A) exhibit lower S_{BET} values, whereas the @CuMgAl-LDHs with 0.10, 0.20 and 0.50 (group B) Cu/Mg molar ratios have higher S_{BET} values. This can be explained by the effectiveness of the removal of the silica core from the SiO_2@CuMgAl-LDHs. It is clearly visible that in group A, the process of leaching the silica core was more effective than in group B (despite applying the same conditions). The lower level of silica core leaching in group B probably leads to the creation of new textured surfaces (more porous) inside the core–shell particles, which leads to an increase in S_{BET}. In group A, it can be taken that greater removal of the SiO_2 core is achieved, which leads to a less porous SiO_2 species.

Spherical @CuMgAl-MO catalysts

After calcination of the LDHs at 450 °C, all characteristic peaks of the double layered structure disappeared and XRD patterns (Fig. 5) show the presence of a poorly crystalline MgO periclase phase with three characteristic diffraction lines at 2θ of approximately 35.1, 43.2 and 62.5° (PDF card no. 00-004-0829). For all the MOs, a slight shift of the reflections with respect to pure MgO is evident. However, irrespective of the Cu content, no highly crystalline Cu-oxide phases (*e.g.*, Cu_2O, CuO) were noted. Additionally, neither was a well-defined $CuAl_2O_4$ spinel phase detected since the calcination temperature is too low.[65–67] Therefore, these observations indicate that the Cu and Al species should be well dispersed in the MgO matrix, forming a solid solution, or that well-dispersed Cu-contained phases under XRD detection limit are formed.[54,62,68] With an increase in the Cu/Mg molar ratio, the diffraction lines become less pronounced, indicating a decrease in the crystallinity of the MOs.[69] However, a large dependence between the intensity of the above-mentioned reflections and the calculated Si/(Si + Cu + Mg + Al) molar ratio was not found.

The shape of the @CuMgAl-MOs N_2 adsorption isotherms did not change notably in comparison to the pristine LDH-based materials (Fig. 6), implying that the mesoporous character of the hollow spheres with slit-like pores was preserved after heat treatment. In turn, all designated textural parameters (we did not consider V_{micro}, which has a negligible impact on

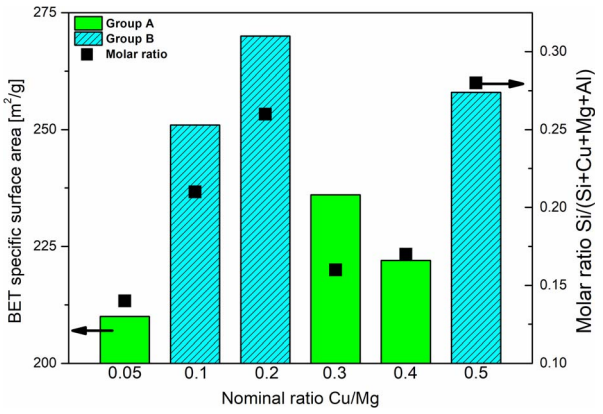

Fig. 4 Correlation between the degree of SiO_2 core etching and the textural properties of the @CuMgAl-LDHs.

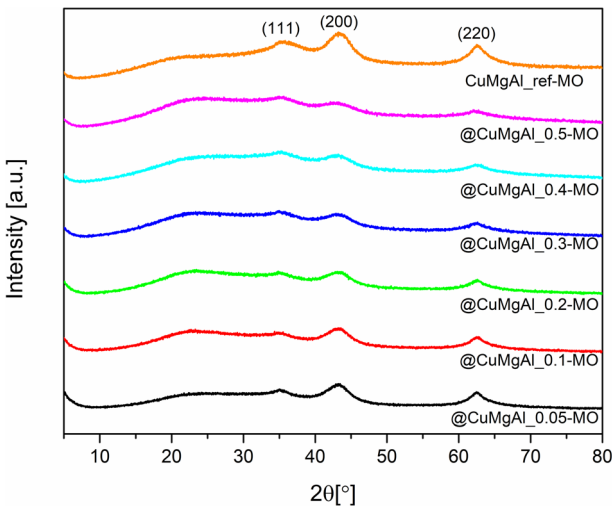

Fig. 5 XRD patterns of the @CuMgAl-MO systems and CuMgAl-MO reference catalyst.

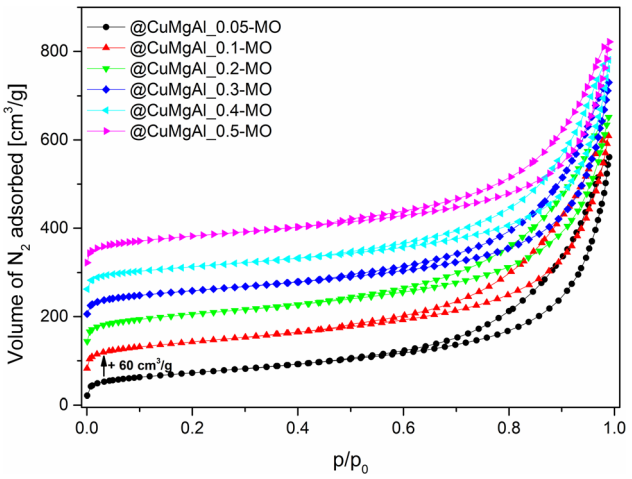

Fig. 6 N_2 adsorption isotherms of the @CuMgAl-MO catalysts.

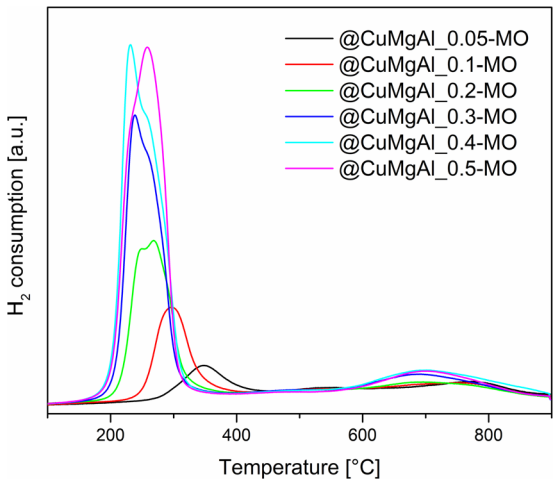

Fig. 7 H_2-TPR profiles of the @CuMgAl-MO systems pre-treated at 450 °C.

the total porosity of studied materials, Table 4) increased after transformation of the LDHs to the MOs, which is in line with the literature.[70–72] We noted a growth in the specific surface area by 14–24% (S_{BET} = 261–308 $m^2\ g^{-1}$), while maintaining the trend related to the presence of the silica core in the @CuMgAl materials (lower degree of SiO_2 removal means higher S_{BET}). The reported S_{BET} values are approximately two times higher than for similar CuMgAl systems with comparable compositions made at similar annealing temperatures but without spherical ordering.[54,70–74] Therefore, it can be concluded that the formation of mixed oxides from core–shell systems is beneficial to their resulting properties. In turn, the volume of meso- and macropores, as well as total porosity, increased after calcination by an average of 19, 31 and 23%, respectively. Considering that V_{total} was in the range of 0.81–0.87 $cm^3\ g^{-1}$, it can be unequivocally stated that the mesopores (V_{meso} = 0.45–0.54 $cm^3\ g^{-1}$) play a dominant role in the pore systems of the @CuMgAl-MOs, which are supplemented by macroporous voids (V_{macro} = 0.29–0.37 $cm^3\ g^{-1}$).

The reducibility of the @CuMgAl-MO samples was studied using H_2-TPR. The collected TPR profiles show two fundamental peaks of hydrogen consumption (Fig. 7). The first maximum is in the range of 230–350 °C (low-thermal peak), whereas the second one is at approximately 700 °C (high-thermal peak). It can be easily seen that the intensity and position of the observed low-thermal peak depends on the content of Cu in the CuMgAl mixed oxides. An increase in the Cu loading (Cu/Mg molar ratio) resulted in a higher amount of H_2 consumed as well as a shift of the reduction process towards lower temperatures. However, different peak shapes are observed. Above a threshold of Cu/Mg = 0.2, a clear splitting or shouldering of signals is visible. Typically, CuO reduction occurs stepwise, the reduction of Cu^{2+} to Cu^+ is closely followed by the reduction of Cu^+ to Cu^0.[75] Therefore, in our case the low-thermal peak may be attributed to the complete reduction of the Cu^{2+} species incorporated in the MgAl phase to metallic Cu.[76,77] Additionally, the segregated CuO phase present on the surface of the MgAl oxide is rather excluded, since reduction of CuO takes place at lower temperatures.[71,78] The reduction temperature is connected to the strength of interaction between the Cu species and the MgAl matrix. Thus, it seems that Cu^{2+} ions present in the @CuMgAl_MO systems are strongly stabilised against reduction in a Mg-reach MgAl oxide matrix. In our study, reduction begins at temperatures as high as 260 °C (for @CuMgAl_0.05-MO) and gradually drops to 140 °C (for @CuMgAl_0.5-MO). A similar stabilisation of the Cu species deposited on pure MgO and on MgAl mixed oxides was recently reported by Basąg *et al.*[77] and Luggren *et al.*[79] Other possible explanations could be the formation of more aggregated Cu-species (still under XRD detection level) dispersed in the samples that have higher Cu content. Possibly, these more aggregated species are more easily reduced than smaller ones. In turn, the high-thermal H_2-TPR peak observed between 600 and 900 °C, with a maximum at approximately 700 °C, is associated with the reduction of $CuAl_2O_4$ or the more complex

Table 4 Textural properties of the @CuMgAl mixed oxides

Sample	S_{BET} [$m^2\ g^{-1}$]	V_{micro} [$cm^3\ g^{-1}$]	V_{meso} [$cm^3\ g^{-1}$]	V_{macro} [$cm^3\ g^{-1}$]	V_{total} [$cm^3\ g^{-1}$]
@CuMgAl_0.05-MO	261	0.013	0.485	0.370	0.867
@CuMgAl_0.1-MO	294	0.015	0.536	0.297	0.849
@CuMgAl_0.2-MO	308	0.018	0.511	0.293	0.822
@CuMgAl_0.3-MO	283	0.019	0.473	0.357	0.850
@CuMgAl_0.4-MO	262	0.016	0.479	0.341	0.836
@CuMgAl_0.5-MO	296	0.021	0.449	0.335	0.806

Table 5 Redox properties of the calcined @CuMgAl materials

Sample	H_2 consumption [mmol $g_{catalyst}^{-1}$]	$H_{2\ consumed}/H_{2\ theoretical}$
@CuMgAl_0.05-MO	0.28	0.42
@CuMgAl_0.1-MO	0.60	0.58
@CuMgAl_0.2-MO	1.13	0.70
@CuMgAl_0.3-MO	1.90	0.83
@CuMgAl_0.4-MO	2.59	0.96
@CuMgAl_0.5-MO	2.66	0.95

$Cu_{1-x}Mg_xAl_2O_4$ spinel phase.[54,71] However, it should be stressed that the studied materials were prepared by thermal treatment at 450 °C. According to Kovanda *et al.*,[65] a well-defined $CuAl_2O_4$ spinel phase formed from CuMgAl LDHs only appears after calcination above 800 °C. However, it might be that the above-mentioned phase can be formed *in situ* under the conditions of the TPR experiment. On the other hand, the high-temperature peak may also reflect the reaction of H_2 with highly stable carbonates and/or arise from residual template species that do not decompose during thermal treatment at 450 °C. Based on the TPR curves, the total amount of redox sites was calculated from all peaks in the range of 25–900 °C (Table 5). The total number of redox sites increases with the Cu/Mg molar ratio and ranges from 0.28 to 2.66 [mmol $g_{catalyst}^{-1}$]. However, the two samples with the highest nominal Cu/Mg molar ratio (0.4 and 0.5) possess almost identical H_2 consumption values. This can be explained by the comparable Cu content in both @CuMgAl_0.4-MO and @CuMgAl_0.5-MO (17.1 and 16.9 wt% of Cu, respectively), due to the fact that the latter possess more silica in the spherical system (Si/(Si + Cu + Mg + Al) is 0.22 and 0.32, respectively). The calculated values of $H_{2\ consumed}/H_{2\ theoretical}$ were below 1 at all Cu/Mg molar ratios. However, an increase in this value is observed in line with the increase in Cu content (from 0.42 to 0.95). Similar findings were also reported previously for bulky CuMgAl mixed oxides with various Cu loadings[54] and indicate that the copper ions are only partially reduced under the applied experimental conditions. Additionally, the formation of small amounts of Cu_2O during the calcination step cannot be excluded.[80]

Catalytic performance of @CuMgAl-MO

The catalytic performance of the @CuMgAl-MOs as well as a CuMgAl-MO reference material was tested in the NH_3-SCR reaction. The relationship between the NO conversion and N_2 selectivity, N_2 being the desired product, *vs.* temperature is presented in Fig. 8. The influence of the Cu content of the @CuMgAl-MOs on the NO conversion is very visible. The reduction of NO by ammonia in the presence of @CuMgAl-MOs started at around 150 °C and it gradually increased with increasing reaction temperature. Increasing the Cu loading in the @CuMgAl-MOs causes a significant shift of the NO conversion profiles toward lower temperatures. The maximum NO conversion level of 89% was obtained for the @CuMgAl_0.5-MO catalyst at a temperature of 275–300 °C. The increased NO conversion of the @CuMgAl-MOs catalysts at higher Cu/Mg

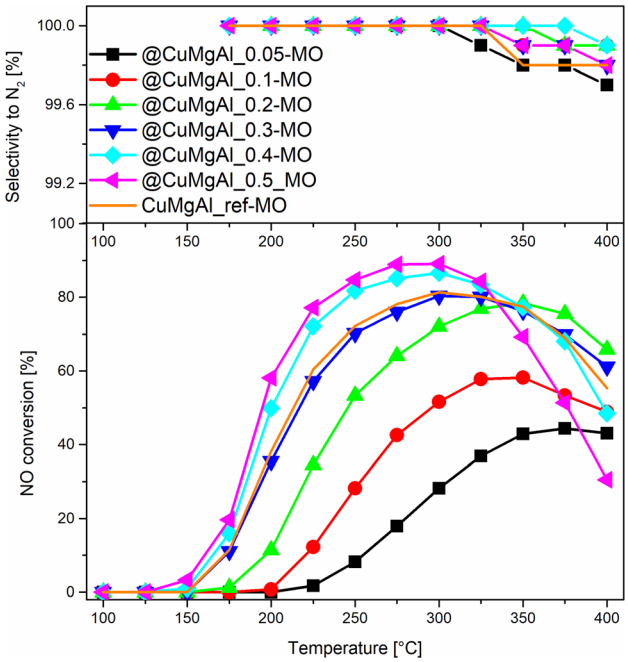

Fig. 8 Results from the NH_3-SCR catalytic tests for the @CuMgAl-MOs and CuMgAl-MO reference catalyst.

molar ratios can be associated with the results of the H_2-TPR measurements, where the copper species were more easily reduced at higher Cu loadings (Fig. 7). However, in the high temperature region, a decrease in the NO conversion, assigned to the side process of direct NH_3 oxidation by O_2, was observed. Additionally, this effect is more pronounced for the MOs that demonstrate higher NO conversions. It should be noted that the N_2 selectivity was studied over the entire temperature range and, regardless of the composition of the @CuMgAl-MO hollow spheres, was found to be very high (over 99.7%), which indicates a high selectivity for NO to N_2 conversion.

To compare the catalytic behaviour of the @CuMgAl-MO hollow sphere catalysts with bulk CuMgAl-MO catalysts, a classical bulk CuMgAl-MO catalyst was prepared by coprecipitation,[81] and both types of catalysts were studied under the same reaction conditions. Although the CuMgAl_ref-MO material possesses a little more Cu content than the @CuMgAl_0.4-MO and @CuMgAl_0.5-MO core–shell catalysts (7.0 *vs.* 5.8 and 5.7 at%, respectively), the former shows a slightly weaker catalytic performance. The NO conversion profile for CuMgAl_ref-MO is most similar to that found for @CuMgAl_0.3-MO. Thus, it can be concluded that the @CuMgAl-MO hollow sphere catalyst demonstrated higher NO conversion than the bulk CuMgAl-MO reference material. The lower NO conversion of bulk CuMgAl-MO may be due to the fact that the Cu-species present in this sample are harder to reduce, as concluded from the H_2-TPR measurements. Moreover, the impact of its poor stone-like morphology, relatively low surface area (S_{BET} = 86 $m^2\ g^{-1}$), poor surface acidity (37.5 μmol g^{-1}, *ca.* five times lower than for the hollow systems) and dissimilar textural properties, which may determine the accessibility of active sites for the reactants, cannot be excluded either.

The comparison of NO conversion rates achieved using the @CuMgAl-MO hollow spheres (a maximum NO conversion level of 89% was obtained using the @CuMgAl_0.5-MO catalyst at a temperature of 275–300 °C) with the values reported in literature is dependent on the different reaction conditions. For example, Wu *et al.*[82] reported about 80% conversion of NO and 75% selectivity to N_2 at a temperature of 250 °C using a CuMgAl catalyst with a molar ratio of Cu : Mg : Al = 2 : 1 : 1. Zhang *et al.*[83] studied a similar system with a molar ratio of Cu : Mg : Al = 1 : 1 : 1 and reported a maximum NO conversion level of 58% at a temperature of 240 °C. In turn, Basąg *et al.*[53] achieved 92% conversion of NO and 96% selectivity to N_2 at a temperature of 325 °C, despite a much lower copper content (Cu : Mg : Al molar ratio equal to *ca.* 0.2 : 1.9 : 1.0). Chmielarz *et al.*[15] studied LDH-derived catalysts with Cu : Mg : Al molar ratios of 0.2 : 2.3 : 1.0, 0.35 : 2.0 : 1.0 and 0.7 : 1.8 : 1.0, which presented NO conversions at 250 °C of 85, 94 and 95%, respectively. The selectivity to nitrogen was above 90% for all these catalysts. However, a drop in the NO conversion at above 250 °C, especially for the catalysts with the highest copper loading, was observed. In the case of binary CuAl catalysts, *ca.* a 70–95% conversion of NO is achieved over temperature ranges of 200–250 °C, depending on the composition and method of catalyst preparation.[84–87]

The catalytic behaviour of the studied catalysts in the side process of direct ammonia oxidation by oxygen was verified by conducting additional catalytic tests. As can be seen in Fig. 9, the catalytic activity of the studied samples increased with an increase in the copper loading. However, what is very important, nearly all ammonia is oxidised to dinitrogen. Thus, residual ammonia, not converted in the NH_3-SCR reaction, could be selectively oxidised to N_2, which is important in the case of the possible ammonia slip.

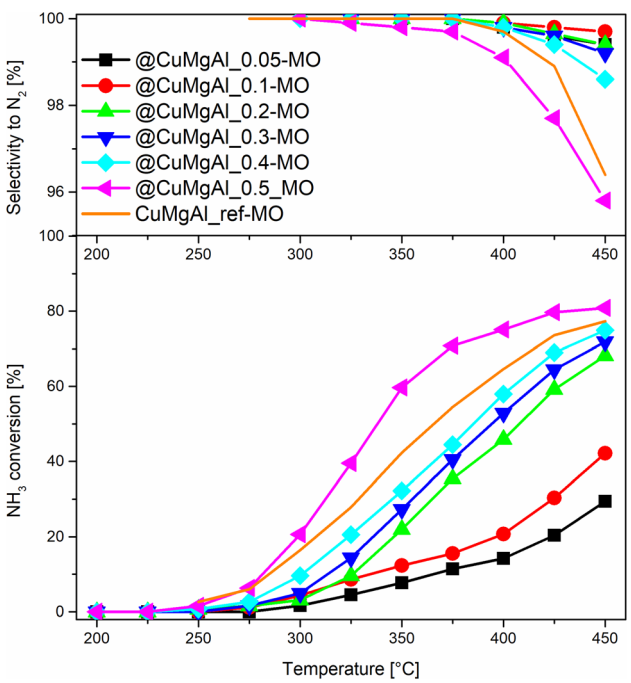

Fig. 9 Results of NH_3 oxidation in the presence of the @CuMgAl-MOs and CuMgAl-MO reference catalysts.

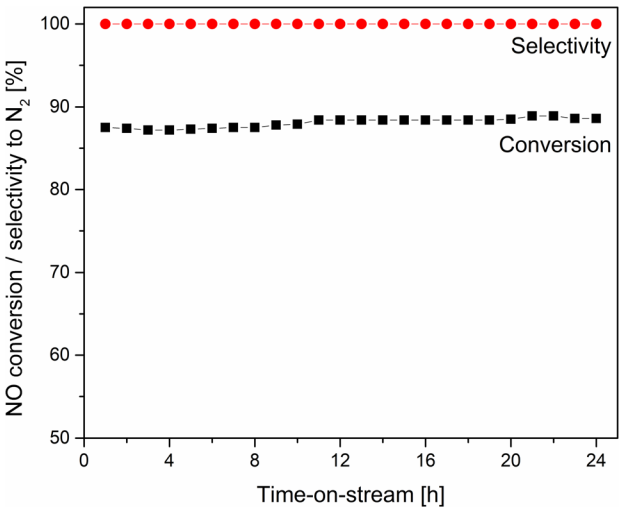

Fig. 10 Results of long-term isothermal NH_3-SCR catalytic test for the @CuMgAl_0.5-MO catalyst at 275 °C.

The stability of the most active NH_3-SCR catalyst (@CuMgAl_0.5-MO) was also examined at 275 °C (Fig. 10). The collected results clearly confirm that no noticeable changes in catalytic efficiency are observed during the 24 hour catalytic run. Over the entire duration of the test, the NO conversion was stable, reaching 87.2–88.9% while the N_2 selectivity was 100%.

Conclusions

The studied materials were found to be active and selective catalysts for a low-temperature selective catalytic reduction of NO_x using ammonia (NH_3-SCR). The activity of the catalysts increases with increasing copper content. Moreover, the temperature window for effective NO conversion is shifted to lower temperatures for the catalysts with the highest copper loadings. Thus, the copper content is very important for the formulation of effective catalysts for the low-temperature NH_3-SCR process. It was shown that the temperature for copper reduction decreases with increasing copper content in the materials. The reducibility of the catalysts is, in general, correlated with their activity in the NH_3-SCR process. Thus, the reducibility of the copper species seems to be very important for the activity of the studied catalysts in the low-temperature range. Comparison of the catalytic performance of the hollow @CuMgAl_0.5_MO sample and a reference catalyst originating from a hydrotalcite mixed metal oxide with a very similar copper loading showed significantly better activity for the hollow sample. These catalysts differ very significantly with respect to their specific surface areas (296 $m^2\ g^{-1}$ for the hollow @CuMgAl_0.5_MO sample *vs.* 86 $m^2\ g^{-1}$ for refence classical hydrotalcite sample). Thus, the surface accessibility of copper is possibly another very important parameter that should be considered when designing effective catalysts for the low-temperature NH_3-SCR process.

Conflicts of interest

There are no conflicts to declare.

Acknowledgements

The authors gratefully thank the Czech Science Foundation of the Czech Republic (Project No. 19-22978S). T. Kondratowicz also thanks European Regional Development Fund-Project "International mobility of employees of the University of Pardubice II" (No. CZ.02.2.69/0.0/0.0/18_053/0016969)". S. Slang thanks used infrastructure (project LM2023037).

References

1 A. Mytareva, D. Bokarev and A. Y. Stakheev, *Kinet. Catal.*, 2021, **62**, 1–32.
2 European Parliament, Council of the European Union, *Directive (EU) 2016/2284 of the European Parilament and of the Council of 14 December 2016 on the reduction of national emissions of certain atmospheric pollutants*, 2016, **https://eur-lex.europa.eu/legal-content/EN/TXT/?uri=uriserv%3AOJ.L_.2016.344.01.0001.01.ENG**.
3 M. Jablonska and R. Palkovits, *Catal. Sci. Technol.*, 2016, **6**, 49–72.
4 L. Han, M. Gao, C. Feng, L. Shi and D. Zhang, *Environ. Sci. Technol.*, 2019, **53**, 5946–5956.
5 P. Wang, L. Yan, Y. Gu, S. Kuboon, H. Li, T. Yan, L. Shi and D. Zhang, *Environ. Sci. Technol.*, 2020, **54**, 6396–6405.
6 L. Kang, L. Han, J. He, H. Li, T. Yan, G. Chen, J. Zhang, L. Shi and D. Zhang, *Environ. Sci. Technol.*, 2018, **53**, 938–945.
7 J.-W. Shi, Y. Wang, R. Duan, C. Gao, B. Wang, C. He and C. Niu, *Catal. Sci. Technol.*, 2019, **9**, 718–730.
8 S. Ali, L. Chen, F. Yuan, R. Li, T. Zhang, X. Leng, X. Niu and Y. Zhu, *Appl. Catal., B*, 2017, **210**, 223–234.
9 F. Liu, W. Shan, Z. Lian, J. Liu and H. He, *Appl. Catal., B*, 2018, **230**, 165–176.
10 H. Chang, T. Zhang, H. Dang, X. Chen, Y. You, J. W. Schwank and J. Li, *Catal. Sci. Technol.*, 2018, **8**, 3313–3320.
11 Y. Zhu, Y. Zhang, R. Xiao, T. Huang and K. Shen, *Catal. Commun.*, 2017, **88**, 64–67.
12 K. Song, C. Gao, P. Lu, D. Ma, Y. Cheng and J.-W. Shi, *Fuel*, 2023, **331**, 125861.
13 Q. Yan, S. Chen, C. Zhang, Q. Wang and B. Louis, *Appl. Catal., B*, 2018, **238**, 236–247.
14 Y. Nie, Q. Yan, S. Chen, D. O'Hare and W. Wang, *Catal. Commun.*, 2017, **97**, 47–50.
15 L. Chmielarz, P. Kuśtrowski, A. Rafalska-Łasocha, D. Majda and R. Dziembaj, *Appl. Catal., B*, 2002, **35**, 195–210.
16 C. Chen, R. Felton, J.-C. Buffet and D. O'Hare, *Chem. Commun.*, 2015, **51**, 3462–3465.
17 Q. Wang and D. O'Hare, *Chem. Commun.*, 2013, **49**, 6301–6303.
18 C. Chen, M. Greenwood, J.-C. Buffet and D. O'Hare, *Green Chem.*, 2020, **22**, 3117–3121.
19 X. Wang, F. Wu, J. Fan, A. Tian, Y. Cheng and S. Yang, *J. Alloys Compd.*, 2021, **888**, 161502.
20 L. Chen, X. Yang, Y. Tian, Y. Wang, X. Zhao, X. Lei and F. Zhang, *Front. Energy Res.*, 2022, **9**, 810568.
21 M. N. Pahalagedara, L. R. Pahalagedara, D. Kriz, S.-Y. Chen, F. Beaulieu, W. Thalgaspitiya and S. L. Suib, *Appl. Catal., B*, 2016, **188**, 227–234.
22 N. I. Blaisi, M. Zubair, S. Ali, T. S. Kazeem, M. S. Manzar, W. Al-Kutti and M. A. Al Harthi, *Environ. Sci. Pollut. Res.*, 2018, **25**, 34319–34331.
23 L. Deng, H. Zeng, Z. Shi, W. Zhang and J. Luo, *J. Colloid Interface Sci.*, 2018, **521**, 172–182.
24 J. Xie, T. Yamaguchi and J.-M. Oh, *J. Solid State Chem.*, 2021, **293**, 121758.
25 M. N. Pahalagedara, L. R. Pahalagedara, C.-H. Kuo, S. Dharmarathna and S. L. Suib, *Langmuir*, 2014, **30**, 8228–8237.
26 G. Varga, Z. Somosi, Z. Kónya, Á. Kukovecz, I. Pálinkó and I. Szilagyi, *J. Colloid Interface Sci.*, 2021, **581**, 928–938.
27 H. Zhang, D. Pan, K. Zou, J. He and X. Duan, *J. Mater. Chem.*, 2009, **19**, 3069–3077.
28 C. Chen, L. K. Yee, H. Gong, Y. Zhang and R. Xu, *Nanoscale*, 2013, **5**, 4314–4320.
29 M. Shao, F. Ning, J. Zhao, M. Wei, D. G. Evans and X. Duan, *J. Am. Chem. Soc.*, 2012, **134**, 1071–1077.
30 S. Zhao, W.-C. Tsen, F. Hu, F. Zhong, H. Liu, S. Wen, G. Zheng, C. Qin and C. Gong, *J. Mater. Sci.*, 2020, **55**, 2967–2983.
31 H. Suo, H. Duan, C. Chen, J.-C. Buffet and D. O'Hare, *RSC Adv.*, 2019, **9**, 3749–3754.
32 F. Mi, X. Chen, Y. Ma, S. Yin, F. Yuan and H. Zhang, *Chem. Commun.*, 2011, **47**, 12804–12806.
33 C. Wang, B. Ma, S. Xu, D. Li, S. He, Y. Zhao, J. Han, M. Wei, D. G. Evans and X. Duan, *Nano Energy*, 2017, **32**, 463–469.
34 Y. Dou, S. Zhang, T. Pan, S. Xu, A. Zhou, M. Pu, H. Yan, J. Han, M. Wei and D. G. Evans, *Adv. Funct. Mater.*, 2015, **25**, 2243–2249.
35 R. Li, T. Xue, R. Bingre, Y. Gao, B. Louis and Q. Wang, *ACS Appl. Mater. Interfaces*, 2018, **10**, 34834–34839.
36 M. Lyu, C. Chen, J.-C. Buffet and D. O'Hare, *New J. Chem.*, 2020, **44**, 10095–10101.
37 Y. Ni, L. Yao, Y. Wang, B. Liu, M. Cao and C. Hu, *Nanoscale*, 2017, **9**, 11596–11604.
38 T. Kondratowicz, S. Slang, L. Dubnová, O. Kikhtyanin, P. Bělina and L. Čapek, *Appl. Clay Sci.*, 2022, **216**, 106365.
39 M. Shirotori, S. Nishimura and K. Ebitani, *J. Mater. Chem. A*, 2017, **5**, 6947–6957.
40 M. Shirotori, S. Nishimura and K. Ebitani, *RSC Adv.*, 2018, **8**, 28024–28031.
41 C. Chen, P. Wang, T.-T. Lim, L. Liu, S. Liu and R. Xu, *J. Mater. Chem. A*, 2013, **1**, 3877–3880.
42 W. L. Kwok, D.-G. Crivoi, C. Chen, J.-C. Buffet and D. O'Hare, *Dalton Trans.*, 2018, **47**, 143–149.
43 D. Cosano, D. Esquivel, A. J. Puertas, F. J. Romero-Salguero, C. Jiménez-Sanchidrián and J. R. Ruiz, *Microporous Mesoporous Mater.*, 2021, **323**, 111247.
44 K. Wang, X. Huang, Y. Liu, W. Fei and Z. Gu, *J. Nanopart. Res.*, 2020, **22**, 1–14.

45 W. Stober, A. Fink and E. Bohn, *J. Colloid Interface Sci.*, 1968, **26**, 1973.
46 X. Chen, F. Mi, H. Zhang and H. Zhang, *Mater. Lett.*, 2012, **69**, 48–51.
47 C. Zhang, M. Shao, L. Zhou, Z. Li, K. Xiao and M. Wei, *ACS Appl. Mater. Interfaces*, 2016, **8**, 33697–33703.
48 M. Shao, F. Ning, Y. Zhao, J. Zhao, M. Wei, D. G. Evans and X. Duan, *Chem. Mater.*, 2012, **24**, 1192–1197.
49 K. Wang, Q. Mao, W. Fei, L. Kong, X. Cao and Z. Gu, *RSC Adv.*, 2021, **11**, 8375–8383.
50 H. Suo, C. Chen, J.-C. Buffet and D. O'Hare, *Dalton Trans.*, 2018, **47**, 16413–16417.
51 M. Liu, H. Wang, P. Zhu, J. Wang, H. Tan and Z. Zheng, *Catal. Commun.*, 2019, **129**, 105752.
52 Y. Shao, K. Sun, Q. Li, Q. Liu, S. Zhang, Q. Liu, G. Hu and X. Hu, *Green Chem.*, 2019, **21**, 4499–4511.
53 S. Basąg, K. Kocoł, Z. Piwowarska, M. Rutkowska, R. Baran and L. Chmielarz, *React. Kinet. Mech. Catal.*, 2017, **121**, 225–240.
54 S. Tanasoi, N. Tanchoux, A. Urdă, D. Tichit, I. Săndulescu, F. Fajula and I.-C. Marcu, *Appl. Catal., A*, 2009, **363**, 135–142.
55 C. Johnson and F. Glasser, *Clay Miner.*, 2003, **51**, 1–8.
56 N. Abushrenta, X. Wu, J. Wang, J. Liu and X. Sun, *Sci. Rep.*, 2015, **5**, 1–9.
57 G. Mitran, T. Cacciaguerra, S. Loridant, D. Tichit and I.-C. Marcu, *Appl. Catal., A*, 2012, **417**, 153–162.
58 G. Cui, F. Wang, S. He and M. Wei, *RSC Adv.*, 2016, **6**, 105406–105411.
59 T. Kondratowicz, M. Drozdek, A. Rokicińska, P. Natkański, M. Michalik and P. Kuśtrowski, *Microporous Mesoporous Mater.*, 2019, **279**, 446–455.
60 J. J. Creasey, A. Chieregato, J. C. Manayil, C. M. Parlett, K. Wilson and A. F. Lee, *Catal. Sci. Technol.*, 2014, **4**, 861–870.
61 L. Smoláková, K. Frolich, J. Kocík, O. Kikhtyanin and L. Čapek, *Ind. Eng. Chem. Res.*, 2017, **56**, 4638–4648.
62 S. Kannan, A. Dubey and H. Knozinger, *J. Catal.*, 2005, **231**, 381–392.
63 Z. Gu, J. J. Atherton and Z. P. Xu, *Chem. Commun.*, 2015, **51**, 3024–3036.
64 M. Thommes, K. Kaneko, A. V. Neimark, J. P. Olivier, F. Rodriguez-Reinoso, J. Rouquerol and K. S. Sing, *Pure Appl. Chem.*, 2015, **87**, 1051–1069.
65 F. Kovanda, K. Jirátová, J. Rymeš and D. Koloušek, *Appl. Clay Sci.*, 2001, **18**, 71–80.
66 M. Salavati-Niasari, F. Davar and M. Farhadi, *J. Sol-Gel Sci. Technol.*, 2009, **51**, 48–52.
67 J. Yanyan, L. Jinggang, S. Xiaotao, N. Guiling, W. Chengyu and G. Xiumei, *J. Sol-Gel Sci. Technol.*, 2007, **42**, 41–45.
68 C. A. Antonyraj, M. Gandhi and S. Kannan, *Ind. Eng. Chem. Res.*, 2010, **49**, 6020–6026.
69 N. Blanch-Raga, A. E. Palomares, J. n. Martínez-Triguero, G. Fetter and P. Bosch, *Ind. Eng. Chem. Res.*, 2013, **52**, 15772–15779.
70 K. A. Ferreira, N. F. Ribeiro, M. M. Souza and M. Schmal, *Catal. Lett.*, 2009, **132**, 58–63.
71 P. Benito, A. Vaccari, C. Antonetti, D. Licursi, N. Schiarioli, E. Rodriguez-Castellón and A. M. R. Galletti, *J. Clean. Prod.*, 2019, **209**, 1614–1623.
72 H. Zhang, Q. Jia, F. Yan and Q. Wang, *Green Energy Environ.*, 2022, **7**, 105–115.
73 J. Shi, Y. He, K. Ma, S. Tang, C. Liu, H. Yue and B. Liang, *Catal. Today*, 2021, **365**, 318–326.
74 O. M. Perrone, F. Lobefaro, M. Aresta, F. Nocito, M. Boscolo and A. Dibenedetto, *Fuel Process. Technol.*, 2018, **177**, 353–357.
75 Z. Liu, M. D. Amiridis and Y. Chen, *J. Phys. Chem. B*, 2005, **109**, 1251–1255.
76 J. Han, H.-Y. Zeng, S. Xu, C.-R. Chen and X.-J. Liu, *Appl. Catal., A*, 2016, **527**, 72–80.
77 S. Basąg, Z. Piwowarska, A. Kowalczyk, A. Węgrzyn, R. Baran, B. Gil, M. Michalik and L. Chmielarz, *Appl. Clay Sci.*, 2016, **129**, 122–130.
78 X.-Y. Xi, Z.-H. Sun, H.-T. Cao, Y.-T. Pei, G. H. ten Brink, P. J. Deuss, K. Barta and H. J. Heeres, *Catalysts*, 2020, **10**, 996.
79 P. J. Luggren, C. R. Apesteguia and J. I. Di Cosimo, *Appl. Catal., A*, 2015, **504**, 256–265.
80 B. Montanari, A. Vaccari, M. Gazzano, P. Käßner, H. Papp, J. Pasel, R. Dziembaj, W. Makowski and T. Lojewski, *Appl. Catal., B*, 1997, **13**, 205–217.
81 F. Kovanda, E. Jindova, B. Dousova, D. Kolousek, J. Plestil and Z. Sedlakova, *Acta Geodyn. Geomater.*, 2009, **6**, 111–119.
82 X. Wu, J. Liu, X. Liu, X. Wu and Y. Du, *J. Catal.*, 2022, **407**, 265–280.
83 Y.-S. Zhang, C. Li, C. Yu, T. Tran, F. Guo, Y. Yang, J. Yu and G. Xu, *Chem. Eng. J.*, 2017, **330**, 1082–1090.
84 Q. Yan, Y. Nie, R. Yang, Y. Cui, D. O'Hare and Q. Wang, *Appl. Catal., A*, 2017, **538**, 37–50.
85 Q. Yan, Y. Gao, Y. Li, M. A. Vasiliades, S. Chen, C. Zhang, R. Gui, Q. Wang, T. Zhu and A. M. Efstathiou, *Appl. Catal., B*, 2019, **255**, 117749.
86 H. Meng, J. Liu, Y. Du, B. Hou, X. Wu and X. Xie, *Catal. Commun.*, 2019, **119**, 101–105.
87 W. Wang, L. Wang, Y. Rao, Y. Huang, R. Li, F. Wei, H. Mei and J. Cao, *Appl. Surf. Sci.*, 2023, **618**, 156638.